PAPER

Valence subbands profile regulation in AlGaN quantum well based on $k \cdot p$ theory

Physica Scripta

PAPER

Valence subbands profile regulation in AlGaN quantum well based on $k{\cdot}p$ theory

Xianjun Wang[1,2], **Ke Jiang**[1,2], **Xiaojuan Sun**[1,2], **Zi-Hui Zhang**[1,3], **Yuxuan Chen**[1,2], **Bingxiang Wang**[1,2] and **Dabing Li**[1,2]

[1] State Key Laboratory of Luminescence and Applications, Changchun Institute of Optics, Fine Mechanics and Physics, Chinese Academy of Sciences, Changchun 130033, People's Republic of China
[2] Center of Materials Science and Optoelectronics Engineering, University of Chinese Academy of Sciences, Beijing 100049, People's Republic of China
[3] Key Laboratory of Electronic Materials and Devices of Tianjin, School of Electronics and Information Engineering, Hebei University of Technology, Tianjin 300401, People's Republic of China

E-mail: jiangke@ciomp.ac.cn **and** lidb@ciomp.ac.cn

RECEIVED
30 August 2022

REVISED
13 January 2023

ACCEPTED FOR PUBLICATION
2 February 2023

PUBLISHED
15 February 2023

Keywords: quantum well, AlGaN, ***k•p*** theory, strain, sub-bands

Abstract

The profiles for the valence subbands of an AlGaN-based quantum well (QW) is investigated by considering quantum confinement effect (QCE) and strain through the ***k·p*** theory. We have found that to increase the QCE and the compressive strain would rise the relative position of the heavy hole (HH) subband to the crystal field splitting hole (CH) subband in the valence band of the QW. However, although the variation trend of the relative valance subbands position is similar, the underlying mechanisms of the modulation by the QCE and strain are not the same. In addition, we have found that if the energy level between the HH and the CH subbands is close at a certain $\boldsymbol{k_t}$ point, the subband anti-crossing effect of the QW will enhance their coupling level, causing dipole moments from the conduction subbands to these valence subbands transformation between each other. These results can provide important basis for the active region design of some AlGaN-based short wavelength, high carrier injection, or monolithic integration optoelectronic devices.

1. Introduction

Deep ultraviolet (DUV) light sources have important applications in biomedical disinfection, medical treatment, information communication, and so on [1–7]. Among the candidates that can generate DUV light, AlGaN-based DUV light-emission diode (LED) is one of the most promising solid-state light sources at the present stage because of its direct and adjustable ultra-wide band gap from 3.4 to 6.2 eV, corresponding to the working wavelength from 365 to 210 nm, with Al composition [5, 6]. However, when the emission wavelength of AlGaN-based LED is in the DUV band, especially below 250 nm, the external quantum efficiency (EQE) will decrease dramatically [8–10]. As for Al-rich AlGaN, except for poor crystal quality and low doping efficiency [8, 11], the difficulty for extracting the photons from the QWs also takes the responsivity for the low EQE [12]. The reason is that, with the Al content increasing, the intensity of transverse electric (TE) field polarized light propagating along *c*-axis decreases obviously, while that of transverse magnetic (TM) field polarized light, propagating perpendicularly to the *c*-axis, escaping from the sidewalls, enhances [8, 12–16]. From this point of view, it is necessary to improve the TE-polarized light intensity. On the other side, however, as a very hot and promising topic, monolithic photonics integration circuit (PIC) requires the light to propagate and couple laterally [17–19]. Consequently, it is necessary to improve the TM-polarized light intensity, instead. In short, to investigate the regulation methods of the TE/TM polarization ratio for AlGaN-based DUV LED is important for their applications.

In the wurtzite AlGaN material, under the crystal field and spin–orbit coupling, the valence band contains heavy hole (HH), light hole (LH), and crystal field splitting hole (CH) subbands [15, 20]. The luminescence of AlGaN-based DUV LED mainly comes from the electron-hole recombination between conduction subband

and valence subband in the QWs. The conduction subbands consist of symmetrical ***S*** orbitals, so the polarization characteristics of photons produced by the transition from different conduction bands to the same valence subband will not change. However, due to the asymmetry of wurtzite crystal field and spin–orbit coupling, the ***P*** orbit of valence band is asymmetric. Hence, the transition from conduction subband to different valence subbands will produce photons with different polarizations [21]. Since the transition probability between the conduction and top valence subband is larger than that between the conduction and bottom valence subband, the profiles for the valence subbands largely determine the interband transition polarization characters. Accordingly, to regulate the valence subband configuration of the QWs is the method to fundamentally adjust the optical TE/TM polarization ratio of the AlGaN-based DUV LEDs.

Previous studies have shown that to change the QCE of the QWs including the space and potential confinements and to vary the in-plane strain can modify the profiles for valence subbands [22–29]. However, for III-nitrides, there is always a correlation between the QCE and the in-plane strain due to the coherent existence of piezoelectric and spontaneous polarization field, meaning that only a single parameter change of the QW structure such as Al-content, well or barrier width, or elastic constants, will result in another changes such as interface charge, potential, or strain states, which causes that the independent effects of the QCE and the strain on the valance subband structures are not clear till now. In this work, we have separately studied the effects of QCE and strain on the valence subband profiles based on the ***k·p*** theory. We find that both enhancement of QCE and compressive strain are helpful to rise the HH subband position relative to CH subband, enhancing the TE spontaneous emission rate and weakening the TM spontaneous emission rate. It is noteworthy that if the energy levels of these valance subbands are close, the coupling effect will enhance, leading to the light polarization conversion with increasing wave vector. These results can provide important basis for the active region design of some AlGaN-based short wavelength, high carrier injection, or monolithic integration optoelectronic devices.

2. *k●p* theory and simulations

The 6×6 Hamiltonian matrix ***k·p*** method is used to calculate the valance subbands [21]. After diagonalizing, the 6×6 Hamiltonian matrix can be expressed by upper and lower Hamiltonians as equation (1):

$$H_{6\times6} = \begin{bmatrix} H^U_{3\times3} & 0 \\ 0 & H^L_{3\times3} \end{bmatrix}. \tag{1}$$

The hole wavefunctions are expressed as following equations (2):

$$\psi^U_m(z;\, k_t) = \frac{e^{ik_t\cdot r_t}}{\sqrt{A}}(g^{(1)}_m(z;\, k_t)|1\rangle + g^{(2)}_m(z;\, k_t)|2\rangle + g^{(3)}_m(z;\, k_t)|3\rangle), \tag{2a}$$

$$\psi^L_m(z;\, k_t) = \frac{e^{ik_t\cdot r_t}}{\sqrt{A}}(g^{(4)}_m(z;\, k_t)|4\rangle + g^{(5)}_m(z;\, k_t)|5\rangle + g^{(6)}_m(z;\, k_t)|6\rangle). \tag{2b}$$

where $k_t = \sqrt{{k_x}^2 + {k_y}^2}$ is the wave vector of the $k_x - k_y$ plane, $g^{(i)}_m(z;\, k_t)$, $i = 1 \sim 6$ is the envelope function of the m-th valence band, $|i\rangle$, $i = 1 \sim 6$ are the bases of the Hamiltonian matrix, and $\sqrt{A}$ is the normalization coefficient. Note that, the axial approximation is used in this study [30], and $\boldsymbol{k_t}$ is isotropic in the plane, therefore, we only care about the magnitude of $\boldsymbol{k_t}$ is used in the calculation. Because the QW is inversion symmetry, the upper and lower Hamiltonians have the same energy band structure. Thus, only the upper Hamiltonian matrix is considered. The effective mass equation of the upper Hamiltonian matrix $H^U_{3\times3}$ of the valence band is expressed as the following equation (3):

$$\sum_{j=1}^{3}\left[H^U_{lj}\left(k_z = -i\frac{\partial}{\partial z}\right) + \delta_{lj}E^0_v(z)\right]g^{(l)}_m(z;\, k_t) = E^U_m(k_t)g^{(l)}_m(z;\, k_t),\ \ l = 1,\ 2,\ 3. \tag{3}$$

where the bases of $g^{(1)}_m(z;\, k_t)$, $g^{(2)}_m(z;\, k_t)$ and $g^{(3)}_m(z;\, k_t)$ are the $|1\rangle$, $|2\rangle$, and $|3\rangle$, respectively. $|1\rangle$ and $|2\rangle$ are the combinations of $|X\rangle$ and $|Y\rangle$, and $|3\rangle$ only includes $|Z\rangle$. $|X\rangle$, $|Y\rangle$, and $|Z\rangle$ are the wavefunction of ***P*** orbit.

The electron wavefunction is expressed as the following equation (4):

$$\psi^C_n(z;\, k_t) = \frac{e^{ik_t\cdot r_t}}{\sqrt{A}}\phi_n(z)|S,\ \eta\rangle. \tag{4}$$

in which $|S,\ \eta\rangle$ is the wavefunction of ***S*** orbit in the conduction band, η is the spin orientation, and $\phi_n(z)$ is the n-th conduction band envelop function. The effective mass equation for the conduction band is shown as the following equation (5):

$$\left[-\frac{\hbar^2}{2m_e^z}\frac{\partial^2}{\partial z^2}+\frac{\hbar^2 k_t^2}{2m_e^t}+E_c^0(z)\right]\phi_n(z)=E_n^c(k_t)\phi_n(z). \tag{5}$$

where m_e^z and m_e^t are the effective masses at $\boldsymbol{z}$ direction and $\boldsymbol{x}$-$\boldsymbol{y}$ plane, respectively.

In the AlGaN QW, the conduction subbands to valence subbands transition radiates photons with different polarization. The dipole moment M_{nm}^{TE} is for TE-polarized photon and M_{nm}^{TM} is for TM-polarized photon [20, 31]. They are formulated by equations (6):

$$M_{nm}^{TE}=\frac{3}{4}M_b^{TE}\cdot[|\langle\phi_n(z)|g_m^{(1)}(z;\,k_t)\rangle|^2+|\langle\phi_n(z)|g_m^{(2)}(z;\,k_t)\rangle|^2], \tag{6a}$$

$$M_{nm}^{TM}=\frac{3}{2}M_b^{TM}\cdot[|\langle\phi_n(z)|g_m^{(3)}(z;\,k_t)\rangle|^2]. \tag{6b}$$

where M_b^{TE}/M_b^{TM} are the bulk TE/TM dipole moments, which were defined in [20].

By solving the valence band effective mass equation through finite difference method, the energy eigenvalues of $E_m^1(k_t)$, $E_m^2(k_t)$ and $E_m^3(k_t)$ can be obtained. There exists an infinite number of energy eigenvalue solutions, in which the highest three energy levels of $E_0^1(k_t)$, $E_0^2(k_t)$, and $E_0^3(k_t)$ are the topmost valence subbands. At the center of Brillouin zone ($\boldsymbol{k_t}=0$, namely the Γ point), $E_0^1(0)$ contains only $g_0^{(1)}(z;\,0)$, while $E_0^2(0)$ and $E_0^3(0)$ are the mixture of $g_0^{(2)}(z;\,0)$ and $g_0^{(3)}(z;\,0)$. The $E_0^1(k_t)$ energy level is marked as HH subband. As for the $E_0^2(k_t)$ and $E_0^3(k_t)$ energy levels, if it mainly contains $g_0^{(2)}(z;\,0)$ at the Γ point, it is marked as LH subband, while if it mainly contains $g_0^{(3)}(z;\,0)$ at the Γ point, it is marked as CH subband.

The spontaneous emission rates for TE and TM modes are [30]:

$$\mathrm{r}_{sp}^{TE}(\hbar\omega)=\frac{4n_r\omega e^2}{\pi\hbar c^3\varepsilon_0 m_0^2 L_W}\sum_{n,m}\int_0^\infty\frac{k_t\,dk_t}{2\pi}M_{\mathrm{nm}}^{TE}\frac{\gamma/\pi}{[E_{\mathrm{nm}}(k_t)-\hbar\omega]^2+\gamma^2}f_c^n(1-f_v^{ml}) \tag{7a}$$

$$\mathrm{r}_{sp}^{TM}(\hbar\omega)=\frac{4n_r\omega e^2}{\pi\hbar c^3\varepsilon_0 m_0^2 L_W}\sum_{n,m}\int_0^\infty\frac{k_t\,dk_t}{2\pi}M_{nm}^{TM}\frac{\gamma/\pi}{[E_{nm}(k_t)-\hbar\omega]^2+\gamma^2}f_c^n(1-f_v^{ml}) \tag{7b}$$

in which

$$f_c^n=\frac{1}{1+e^{(E_n(k_t)-E_{Fn})/k_BT}},\ f_v^{ml}=\frac{1}{1+e^{(E_m^l(k_t)-E_{Fp})/k_BT}},$$
$$E_{nm}(k_t)=E_n^c(k_t)-E_m^l(k_t) \tag{7c}$$

where f_c^n and f_v^m is the Fermi–Dirac distribution function of n-th conduction subband ($E_n^c(k_t)$) and m-th valence subbands ($E_m^l(k_t)$), n_r is the refractive index, ω is the angular frequency of the optical wave, e is the electronic charge, c is the velocity of light in vacuum, ε_0 is the dielectric constant of vacuum, m_0 is the electronic mass, γ is the constant half width of the Lorentzian shape function, E_{Fn} and E_{Fp} are the quasi-Fermi levels of electrons and holes respectively.

Accordingly, near the Γ point, since the HH subband mainly includes $g_0^{(1)}(z;\,0)$, the TE dipole moment is much large than the TM one, and the TE polarized photons are mainly generated by the transition from conduction band to HH subband. While, since the CH subband mainly includes $g_0^{(3)}(z;\,0)$, the TM dipole moment is lager and the TM polarized photons are mainly generated by the transition from conduction band to CH subband. As a result, it is easy to see that the order of valence subbands has a great influence on the polarization of the emitted photons.

In order to separately investigate the impacts of the QCE and the strain, the upper Hamiltonian matrix $H_{3\times3}^U$ can be written in two terms as the following equation (8) [21]:

$$H_{3\times3}^U=H_0^U+H_{strain}^U=H_0^U+\begin{bmatrix}\lambda_\varepsilon+\theta_\varepsilon & 0 & 0\\ 0 & \lambda_\varepsilon+\theta_\varepsilon & 0\\ 0 & 0 & \lambda_\varepsilon\end{bmatrix}. \tag{8}$$

where H_0^U is strain independent, and λ_ε and θ_ε are strain dependent which are determined by the following equations (9):

$$\lambda_\varepsilon=D_1\varepsilon_{zz}+D_2(\varepsilon_{xx}+\varepsilon_{yy}), \tag{9a}$$

$$\theta_\varepsilon=D_3\varepsilon_{zz}+D_4(\varepsilon_{xx}+\varepsilon_{yy}), \tag{9b}$$

$$\varepsilon_{xx}=\varepsilon_{yy}=\frac{a_0-a}{a}, \tag{9c}$$

$$\varepsilon_{zz}=-\frac{2C_{13}}{C_{33}}\varepsilon_{xx}. \tag{9d}$$

where D_1, D_2, D_3, D_4 are the deformation potentials, ε_{xx}, ε_{yy}, ε_{zz} are the strains along $\boldsymbol{x}$, $\boldsymbol{y}$, $\boldsymbol{z}$ directions, a is the relaxed in-plane lattice constant, and C_{13}, C_{33} are the elastic constants, respectively. By tuning the QW in-plane lattice constant a_0, the strain can be adjust.

A single QW structure of $Al_yGa_{1-y}N/Al_xGa_{1-x}N/Al_yGa_{1-y}N$ ($y \geqslant x + 0.05$) is constructed. To independently study the impacts of the QCE on valance subband profiles, the strain is set to be zero by setting the QW in-plane lattice constant to be the same as the relaxed one. Meanwhile, the spontaneous polarization electric field is set to be zero to avoid potential deformation. As for the investigation of the in-plane strain, it is controlled by modifying the lattice constant a_0. The material parameters used in the simulations are from references [31–33].

3. Results and discussion

According to the $\boldsymbol{k \bullet p}$ theory, the quantum structure barrier height and well width can mainly determine its QCE. By adjusting the two parameters, the QCE is controlled so that the valence bands distribution is regulated. According to the Vegrad's Law, the barrier height can be altered by the Al-composition difference between the barrier and well of the quantum structure. Hence, the barrier height is modified by varying the Al-composition of the barrier and well. In the Hamiltonian matrix of the valence band effective mass equation, the effective hole masses of subbands are different. Therefore, with the variation of the barrier Al composition (y), the well Al composition (x), and the well width (L_w), the boundary conditions of the Schrodinger equation is changed, influencing the relative energy eigenvalues of HH and CH subbands. For convenience, the figure of merit that $\Delta E = E_{HH}(0) - E_{CH}(0)$ is calculated to represent the relative energy position for HH and CH subbands. The HH subband is higher than the CH subband if $\Delta E > 0$, and the CH subband is higher than the HH subband if $\Delta E < 0$.

Figure 1 is the calculated variation trend of ΔE at Γ point with well and barrier compositions (x–y) in terms of different well widths ($L_w = 1, 2, 3$ nm, respectively). The dashed lines are the boundaries between areas of $\Delta E < 0$ and $\Delta E > 0$ and the dotted lines are the well and barrier compositions (x–y) emitting the same wavelength. With the increase of the well width L_w, the area of $\Delta E < 0$ increases and that of $\Delta E > 0$ decreases, implying that with the well width L_w increasing some quantum structures of well and barrier composition combinations (x–y) that possess higher HH subband than CH subband ($\Delta E > 0$) will be converted to that possess higher CH subband than HH subband ($\Delta E < 0$). Furthermore, it can also be seen that in any cases of well widths L_w and well Al compositions x, with the increase of barrier Al composition y, ΔE will increase gradually . These results demonstrate that the relative position of the HH and CH subbands can be effectively regulated by tuning the QCE. Consequently, the degree of polarization (DOP) for the emitting photons can also be regulated by tuning the QCE. Besides, it is also noteworthy that at stronger space confinement, the emitting wavelength can be more effectively controlled by the quantum barrier. The quantum structure $Al_yGa_{1-y}N/Al_xGa_{1-x}N/Al_yGa_{1-y}N$ where $x = 0.6$, $y = 0.888$, $L_w = 2$ nm is calculated as reference in the following discussion because the HH subband energy level and CH subband energy level are almost the same at Γ point under these parameters. Then, we take data near this set of parameters and analyze the changes of HH and CH subbands, so as to analyze the reasons for the changes of TE- and TM-polarized emission.

In order to analyze the influences of well width on the valence subbands distribution and to reflect the change of energy level in more detail and obviously, the valence subband structure in $\boldsymbol{k}$ space with different well width of the quantum structure $Al_yGa_{1-y}N/Al_xGa_{1-x}N/Al_yGa_{1-y}N$ where $x = 0.6$, $y = 0.888$ is calculated as shown in figure 2. When the well width is 2 nm, the HH and CH subbands almost coincide at Γ point ($0 < \Delta E < 0.2$ meV, figure 2(b)). When the well width decreases to 1 nm, both HH and CH subbands shift downwards while the CH subband shift much more than the HH subband. As a result, the HH subband is 23.3 meV higher than the CH subband at Γ point ($\Delta E = 23.3$ meV, figure 2(a)). When the well width increases to 3 nm, both HH and CH subbands shift upwards while the CH subband also shift much more than the HH subband. As a result, the HH subband is 22.9 meV lower than the CH subband at Γ point ($\Delta E = -22.9$ meV, figure 2(c)).

On the other hand, in order to investigate the influences of barrier height on the valence subbands distribution in more detail and obviously, the valence subband structure in $\boldsymbol{k}$ space of the quantum structure $Al_yGa_{1-y}N/Al_{0.6}Ga_{0.4}N/Al_yGa_{1-y}N$ with the quantum well width of 2 nm also is calculated as shown in figure 3. Similarly, taking the $Al_{0.888}Ga_{0.112}N/Al_{0.6}Ga_{0.4}N/Al_{0.888}Ga_{0.112}N$ whose ΔE almost equals to zero as the reference, as the barrier Al content decreases from 0.888 to 0.8, the CH subband shift upwards while the HH subband almost keep constant at Γ point, resulting in a negative ΔE of −19.9 meV (figure 3(a)). As the barrier Al-content increases from 0.888 to 1, the CH subband shift downwards while the HH subband also almost keep constant at Γ point, resulting in a positive ΔE of 31.2 meV (figure 3(c)). Consequently, it can be deduced that the QCE including space and barrier confinement effects can modify the valance subbands order to control the DOP for the emitting photons because of the different susceptibility to QCE between CH and HH subbands.

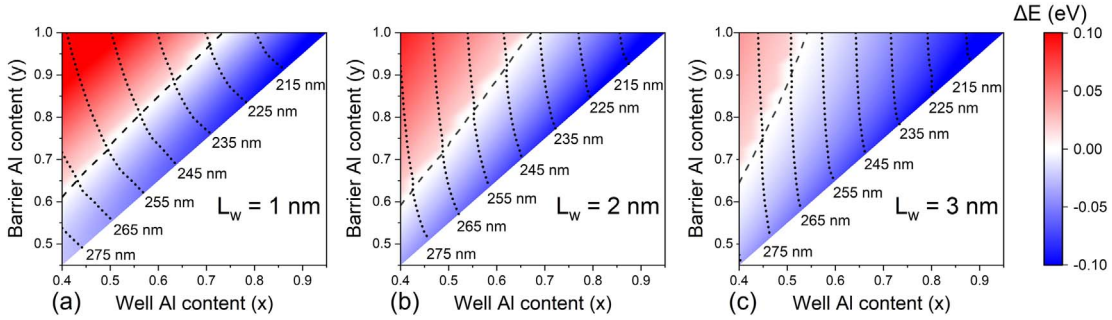

Figure 1. ΔE value under different well and barrier compositions ($x-y$) at a well width of (a) $L_w = 1$ nm, (b) $L_w = 2$ nm, and (c) $L_w = 3$ nm.

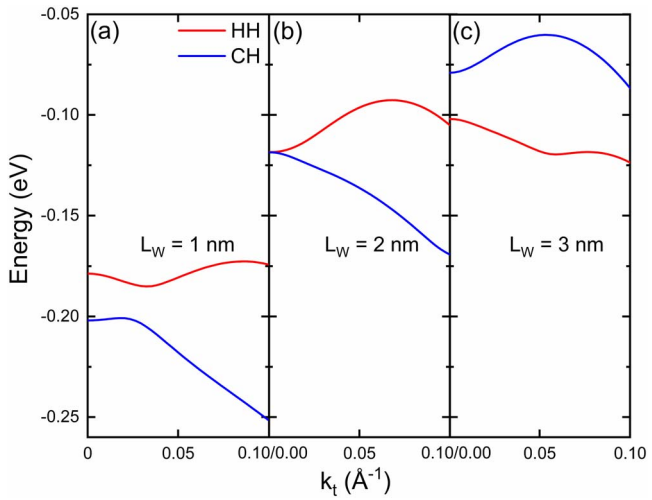

Figure 2. Valence subband structures of $Al_{0.888}Ga_{0.112}N/Al_{0.6}Ga_{0.4}N/Al_{0.888}Ga_{0.112}N$ single well quantum structure with a different quantum well widths of (a) $L_w = 1$ nm, (b) $L_w = 2$ nm, and (c) $L_w = 3$ nm, respectively.

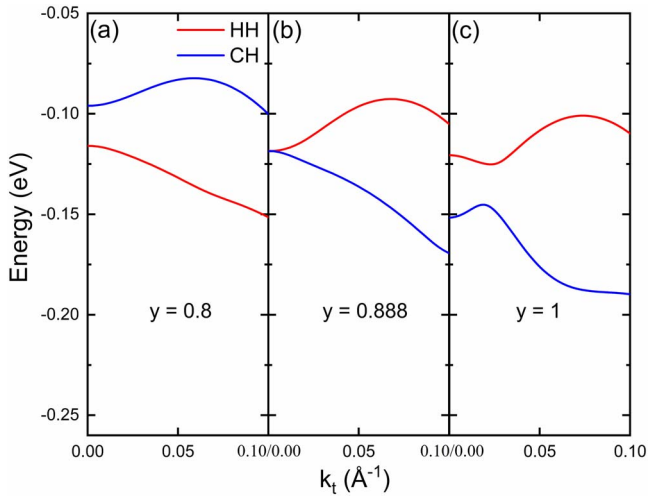

Figure 3. Valence subband structures of $Al_yGa_{1-y}N/Al_{0.6}Ga_{0.4}N/Al_yGa_{1-y}N$ single well quantum structure with well width of 2 nm at different barrier Al contents of (a) y = 0.8, (b) y = 0.888, and (c) y = 1, respectively.

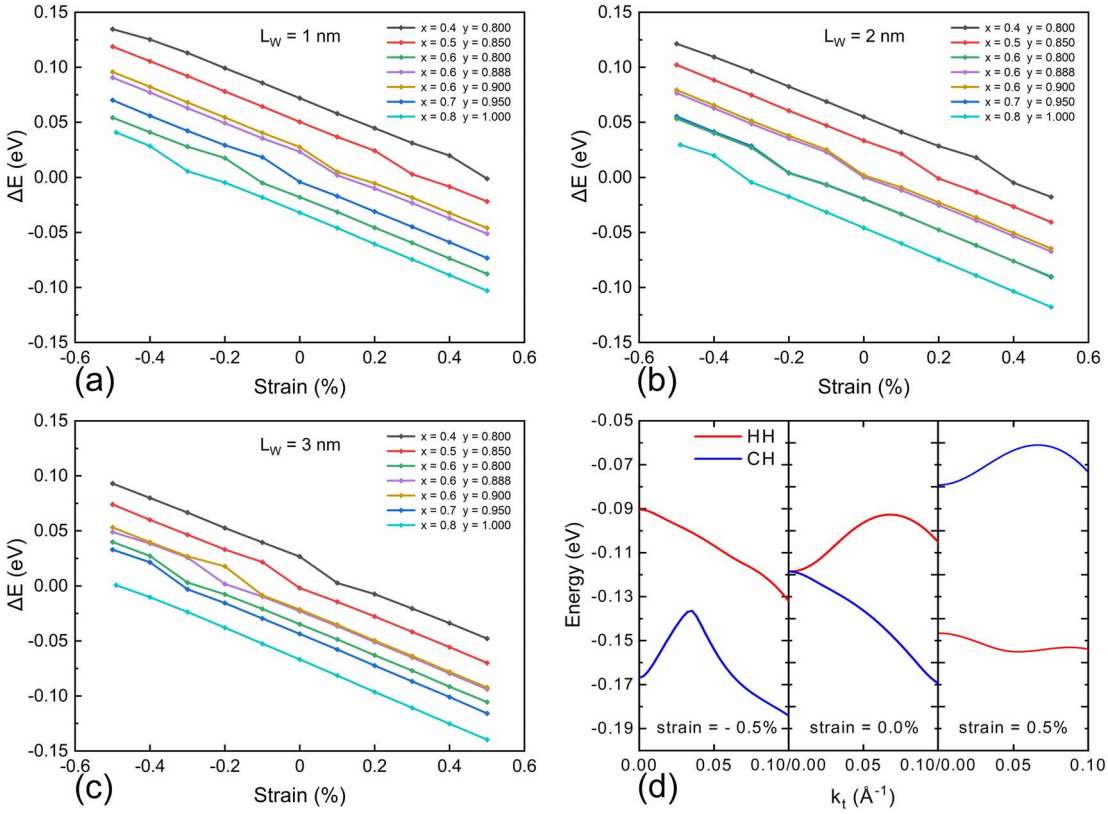

Figure 4. The ΔE variation trends with strain of some different $Al_yGa_{1-y}N/Al_xGa_{1-x}N/Al_yGa_{1-y}N$ quantum structures at the well width of (a) $L_w = 1$ nm, (b) $L_w = 2$ nm, and (c) $L_w = 3$ nm, respectively. (d) Valence subband structures of the $Al_{0.888}Ga_{0.112}N/Al_{0.6}Ga_{0.4}N/Al_{0.888}Ga_{0.112}N$ quantum structure with $L_w = 2$ nm under different strains.

Obviously, the CH subband is more susceptible to QCE than HH subband. Moreover, it seems that the space confinement effect is more beneficial to tune the valance subbands than the barrier confinement effect in AlGaN quantum structures, indicating that it is promising for improving the light extraction efficiency (LEE) of AlGaN based DUV LEDs to develop ultrathin quantum structures.

Figure 4(a)–(c) show the QW energy difference variation trends between HH and CH subbands (ΔE) at Γ point with the biaxial strain for $Al_yGa_{1-y}N/Al_xGa_{1-x}N/Al_yGa_{1-y}N$ quantum structures with different $x-y$ combinations. As it can be seen, at any cases including different well-barrier combinations and well widths, ΔE increases with the increase of compressive strain and decreases with the tensile strain. It means that the compressive strain will make the HH subband move upwards relative to the CH subband, while the tensile strain has the opposite effects on valance subbands in the Al-rich AlGaN quantum structures, indicating the strain is an effective approach to adjust the DOP for the emitting photons. The variation trend of valence band structure with strain is consistent with the results of first principles calculation [34]. Moreover, it can be deduced that to fabricate high compressive AlN template substrate is of importance to improve the LEE of AlGaN-based DUV LEDs. From this point of view, the recently developed high-temperature-annealing (HTA) sputtered AlN/Sapphire template fabrication method, which can provide strong compressive strain to the upper epilayer, is promising in AlGaN based DUV LED fabrication [35–39].

By comparing the absolute value of ΔE and the slope of the lines for each quantum structures with different well width as figure 4(a)–(c), it can be observed that with the well width decrease the absolute value of ΔE gradually increases, while the slope of the lines almost unchanged, indicating the influences of the QCE and the strain on the relative valance subbands are independent. To observe the valance subbands variation with strain more clearly, the HH and CH subbands of the $Al_{0.888}Ga_{0.112}N/Al_{0.6}Ga_{0.4}N/Al_{0.888}Ga_{0.112}N$ quantum structure with $L_w = 2$ nm under compressive strain, unstrain, and tensile strain are extracted as figure 4(d). As is seen, the impact way of strain on the ΔE is different from that of QCE. With the strain varying, both HH and CH subbands change. However, the two subbands shift in opposite directions. When the compressive strain increases, the HH subband shifts upwards while the CH subband shift downwards. When the tensile strain increases, the HH subband shifts downwards while the CH subband shift upwards.

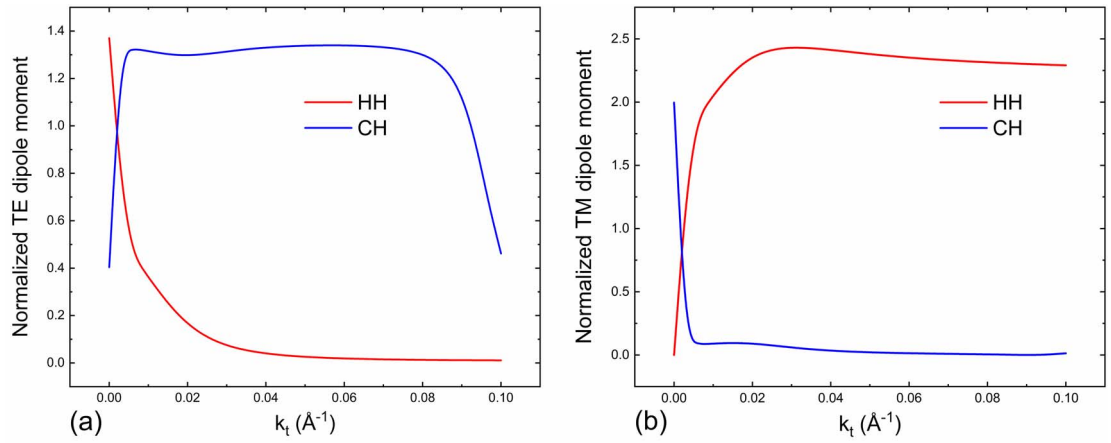

Figure 5. (a) TE and (b) TM dipole moment of the unstrained $Al_{0.888}Ga_{0.112}N/Al_{0.6}Ga_{0.4}N/Al_{0.888}Ga_{0.112}N$ quantum structure with well width of 2 nm.

There is a kind of well-barrier combinations ($x-y$) of a quantum structure whose valance subbands are very close to each other at a certain $\boldsymbol{k_t}$ value like the lines $\Delta E = 0$ shown in figure 1. As is known, when the energy of valence subbands are close to each other at some $\boldsymbol{k_t}$ values, the subbands coupling will become very significant due to the anti-crossing effect in the QW . Hence, the proportion of envelope function in the valence subband wave function will be altered and thus the dipole moment corresponding to its subband will be transformed according to equations (6a) and (b), which will in turn lead to a different TE/TM ratio. Especially when the dipole moment transformation happens near the Γ point and the carrier concentration in the QW is high enough, the transformation will have a great impact on the polarization characteristics of the photons. As for the HH and CH subbands of the $Al_{0.888}Ga_{0.112}N/Al_{0.6}Ga_{0.4}N/Al_{0.888}Ga_{0.112}N$ quantum structure with well width of 2 nm, the energies of HH and CH subbands at Γ point are very close to each other ($0 < \Delta E < 0.5$ meV, figures 2(b), 3(b), 4(d)). With the $\boldsymbol{k_t}$ value increase, as shown in figures 5(a) and (b), the TE dipole moment of the transition from conduction subband to HH subband (C-HH) dramatically decreases and converts to TM one very close to the Γ point. Similarly, the dipole moment of the transition from conduction subband to CH subband (C-CH) also has a rapid conversion from TM to TE mode. Therefore, in the cases of the HH and CH subbands are very close to each other at the Γ point, the polarization characteristics of the emitted photons by the QW will significantly be altered by the injected carrier concentration, which is valuable to some high carrier injection devices such as high-power DUV LEDs or laser diodes (LDs).

To more directly observe the TE and TM emission mode variation with the QCE and strain, the spontaneous emission rate of a series of quantum structures are calculated using equations (7), and the normalized spontaneous emission rate spectra as shown in figure 6. The quantum structure $Al_{0.888}Ga_{0.112}N/Al_{0.6}Ga_{0.4}N/Al_{0.888}Ga_{0.112}N$ with unstrained well of 2 nm is chosen as the reference structure as discussed above (figure 6(a)). Although the energy level of the HH subband is higher than the CH subband as shown in figure 3(b), the spontaneous emission rate of TM-polarized light is higher than that of TE-polarized light, which is resulted from that the anti-crossing effect enhances the coupling effect between the two subbands when the HH and CH subbands are very close to each other. With the decrease of well width, the TE polarization spontaneous emission rate enhances and the TM one reduces relatively (figure 6(c)), coinciding with the valance subbands order variation induced by the well width change (figure 2(a)). Meanwhile, with the increase of barrier height, a similar variation of polarization spontaneous emission rate can be observed (figure 6(e)), which is also coincided with the valance subbands order variation induced by the barrier height change (figure 3(c)). Moreover, with the increase of compressive strain, the TE polarization spontaneous emission rate greatly enhances and the TM one significantly reduces relatively (figures 6(b),(d),(f)), also in well accordance with the valance subbands order variation induced by the strain change (figure 4). The variation trend of TE/TM mode with well width, barrier component and strain calculated in this study is consistent with those reported previously [15, 40–43]. These results directly demonstrate that the QCE and the strain can independently and effectively control the TE/TM polarized luminescence in the Al-rich AlGaN quantum structures through the regulation of valence subband order. By the way, it is noteworthy that the space confinement effect can more seriously impact the emission wavelength, which is important for DUV emission, especially below 250 nm.

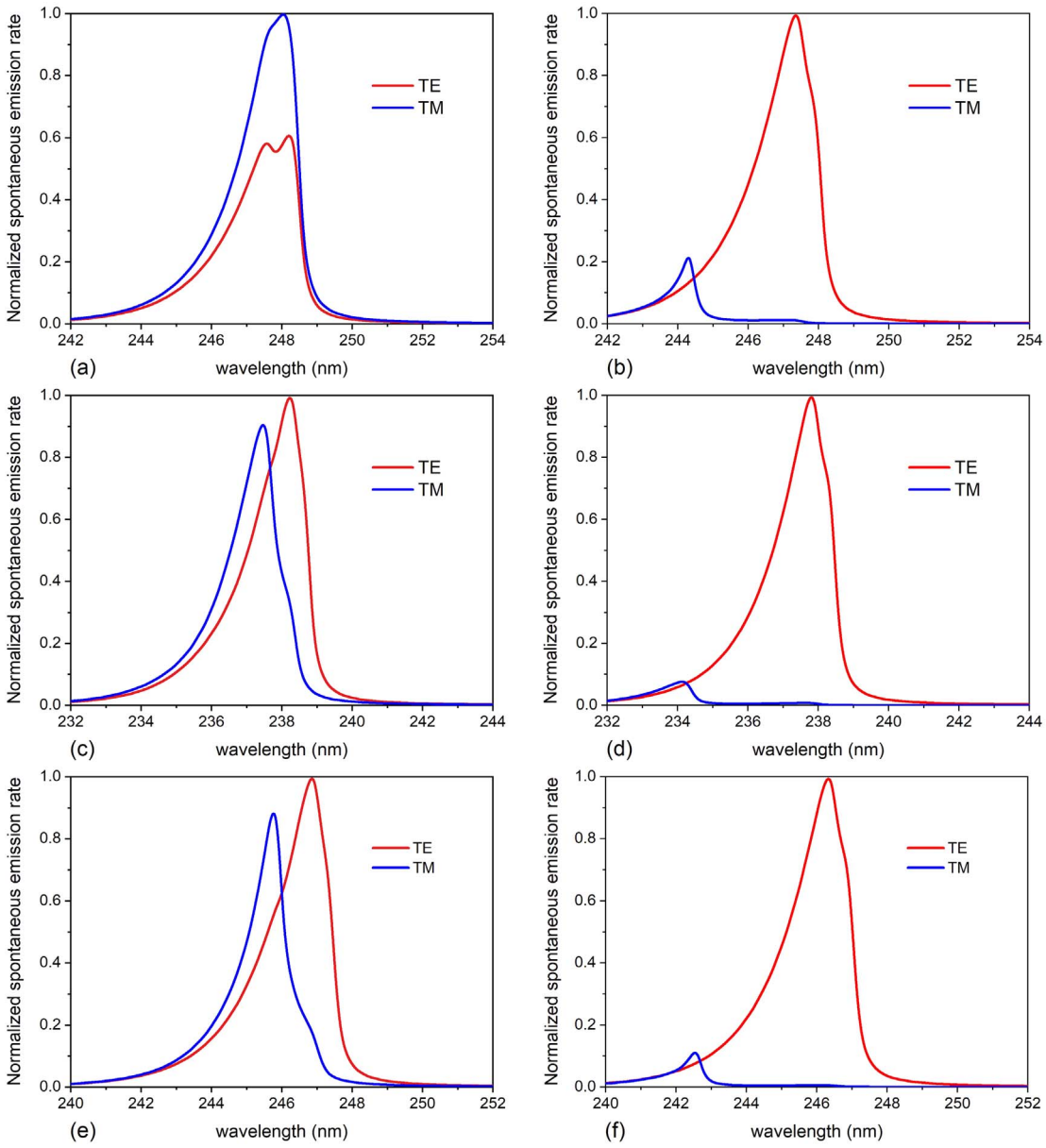

Figure 6. Normalized spontaneous emission rate spectra of the $Al_yGa_{1-y}N/Al_xGa_{1-x}N/Al_yGa_{1-y}N$ quantum structures. The carrier concentrations in the QW are set to be 1×10^{18} cm^{-3}. (a) $x = 0.6$, $y = 0.888$, $L_w = 2$ nm, unstrained; (b) $x = 0.6$, $y = 0.888$, $L_w = 2$ nm, strain of −0.5%; (c) $x = 0.6$, $y = 0.888$, $L_w = 1$ nm, unstraind; (d) $x = 0.6$, $y = 0.888$, $L_w = 1$ nm, strain of −0.5%; (e) $x = 0.6$, $y = 1$, $L_w = 2$ nm, unstrained; (f) $x = 0.6$, $y = 0.888$, $L_w = 2$ nm, strain of −0.5%.

4. Conclusion

In summary, the valence subband profiles in $Al_yGa_{1-y}N/Al_xGa_{1-x}N/Al_yGa_{1-y}N$ ($y \geqslant x + 0.05$) single quantum well is simulated by using $\boldsymbol{k}\cdot\boldsymbol{p}$ theory, and the factors affecting the distribution of valence subbands including the QCE and the strain are separately analyzed. It has been found that the enhancement of the QCE and the compressive strain are both helpful to make the HH subband above the CH subband in the $\boldsymbol{k}$ space, and this will promote the generation of TE-polarized light emission. Oppositely, the decrease of the QCE and increase of the tensile strain can promote the generation of TM-polarized light emission. At a certain $\boldsymbol{k_t}$ value where the anti-crossing effect between valance subbands occurs, the coupling effect will enhance, leading to the light polarization conversion with increasing wave vector $\boldsymbol{k_t}$, indicating the injected carrier concentration may modify the light emission DOP. These results can provide important basis for the active region design of some AlGaN-based short wavelength, high carrier injection, or monolithic integration optoelectronic devices.

Data availability statement

The data that support the findings of this study are available upon reasonable request from the authors.

Funding

This work was supported by the National Natural Science Foundation of China (Nos. 61725403, 62004196, 62121005, 61922078, and 61827813), the Youth Innovation Promotion Association of Chinese Academy of Sciences, and the Youth Talent Promotion Project of the Chinese Institute of Electronics (No. 2020QNRC001).

ORCID iDs

Zi-Hui Zhang https://orcid.org/0000-0003-0638-1118
Dabing Li https://orcid.org/0000-0001-5353-1460

References

[1] Torkzadeh H, Zodrow K R, Bridges W C and Cates E L 2021 Quantification and modeling of the response of surface biofilm growth to continuous low intensity UVC irradiation *Water Res.* **193** 7
[2] Luo X R, Zhang B P, Lu Y H, Mei Y and Shen L 2022 Advances in application of ultraviolet irradiation for biofilm control in water and wastewater infrastructure *J. Hazard. Mater.* **421** 12
[3] Sholtes K and Linden K G 2019 Pulsed and continuous light UV LED: microbial inactivation, electrical, and time efficiency *Water Res.* **165** 10
[4] Razeghi M E 2005 Deep Ultraviolet Light-emitting Diodes and Photodetectors for UV Communications *In: Conf. on Optoelectronic Integrated Circuits VII, (San Jose, CA(US): Spie-Int Soc Optical Engineering)* pp 30–40
[5] Kneissl M, Seong T Y, Han J and Amano H 2019 The emergence and prospects of deep-ultraviolet light-emitting diode technologies *Nat. Photonics* **13** 233–44
[6] Li D B, Jiang K, Sun X J and Guo C L 2018 AlGaN photonics: recent advances in materials and ultraviolet devices *Adv. Opt. Photonics* **10** 43–110
[7] Vitzilaiou E, Kuria A M, Siegumfeldt H, Rasmussen M A and Knochel S 2021 The impact of bacterial cell aggregation on UV inactivation kinetics *Water Res.* **204** 13
[8] Amano H *et al* 2020 The 2020 UV emitter roadmap *J. Phys. D-Appl. Phys.* **53** 57
[9] Kashima Y *et al* 2018 High external quantum efficiency (10%) AlGaN-based deep-ultraviolet light-emitting diodes achieved by using highly reflective photonic crystal on p-AlGaN contact layer *Appl. Phys. Express* **11** 4
[10] Lobo-Ploch N, Mehnke F, Sulmoni L, Cho H K, Guttmann M, Glaab J, Hilbrich K, Wernicke T, Einfeldt S and Kneissl M 2020 Milliwatt power 233nm AlGaN-based deep UV-LEDs on sapphire substrates *Appl. Phys. Lett.* **117** 5
[11] Jiang K, Sun X, Shi Z, Zang H, Ben J, Deng H-X and Li D 2021 Quantum engineering of non-equilibrium efficient p-doping in ultra-wide band-gap nitrides *Light: Science & Applications* **10** 69
[12] Kneissl M and Rass J 2016 *III-Nitride Ultraviolet Emitters: Technology and Applications* (Cham, Switzerland: Springer Cham) 227 (https://doi.org/10.1007/978-3-319-24100-5)
[13] Nam K B, Li J, Nakarmi M L, Lin J Y and Jiang H X 2004 Unique optical properties of AlGaN alloys and related ultraviolet emitters *Appl. Phys. Lett.* **84** 5264–6
[14] Kolbe T, Knauer A, Chua C, Yang Z H, Einfeldt S, Vogt P, Johnson N M, Weyers M and Kneissl M 2010 Optical polarization characteristics of ultraviolet (In)(Al)GaN multiple quantum well light emitting diodes *Appl. Phys. Lett.* **97** 3
[15] Banal R G, Funato M and Kawakami Y 2009 Optical anisotropy in 0001 -oriented $Al_xGa_{1-x}N$/AlN quantum wells ($x > 0.69$) *Phys. Rev. B* **79** 121308
[16] Kawanishi H, Senuma M and Nukui T 2006 Anisotropic polarization characteristics of lasing and spontaneous surface and edge emissions from deep-ultraviolet (lambda approximate to 240 nm) AlGaN multiple-quantum-well lasers *Appl. Phys. Lett.* **89** 3
[17] Huang C, Zhang H C and Sun H D 2020 Ultraviolet optoelectronic devices based on AlGaN-SiC platform: Towards monolithic photonics integration system *Nano Energy* **77** 17
[18] Floyd R, Hussain K, Mamun A, Gaevski M, Simin G, Chandrashekhar M V S and Khan A 2020 Photonics integrated circuits using $Al_xGa_{1-x}N$ based UVC light-emitting diodes, photodetectors and waveguides *Appl. Phys. Express* **13** 4
[19] Alfaraj N, Min Jung W, Kang Chun H, Alatawi Abdullah A, Priante D, Subedi Ram C, Tangi M, Ng Tien K and Ooi Boon S 2019 Deep-ultraviolet integrated photonic and optoelectronic devices: A prospect of the hybridization of group III-nitrides, III-oxides,and two-dimensional materials *J. Semicond.* **40** 1674-4926(2019)40:122.0.TX;2-K
[20] Chuang S L and Chang C S 1996 k center dot p method for strained wurtzite semiconductors *Phys. Rev. B* **54** 2491–504
[21] Chuang S L and Chang C S 1997 A band-structure model of strained quantum-well wurtzite semiconductors *Semicond. Sci. Technol.* **12** 252–63
[22] Lu H M, Yu T J, Yuan G C, Chen X J, Chen Z Z, Chen G X and Zhang G Y 2012 Enhancement of surface emission in deep ultraviolet AlGaN-based light emitting diodes with staggered quantum wells *Opt. Lett.* **37** 3693–5
[23] Lu H, Yu T, Chen X, Wang J and Zhang G 2016 Band engineering for surface emission enhancement in Al-rich AlGaN-based deep-ultraviolet light emitting diodes *Jpn. J. Appl. Phys.* **55** 05fj12
[24] Roberts C, Yan Q M, Miao M S and Van de Walle C G 2012 Confinement effects on valence-subband character and polarization anisotropy in (11(2)over-bar2) semipolar InGaN/GaN quantum wells *J. Appl. Phys.* **111** 4
[25] Tian K K, Chu C S, Che J M, Shao H, Kou J Q, Zhang Y H, Zhou X Y, Feng Z H, Wei T B and Zhang Z H 2019 Interplay between various active regions and the interband transition for AlGaN-based deep-ultraviolet light-emitting diodes to enable a reduced TM-polarized emission *J. Appl. Phys.* **126** 7

[26] Wierer J J Jr, Montano I, Crawford M H and Allerman A A 2014 Effect of thickness and carrier density on the optical polarization of $Al_{0.44}Ga_{0.56}N/Al_{0.55}Ga_{0.45}N$ quantum well layers *J. Appl. Phys.* **115** 174501
[27] Xu H Q, Long H L, Jiang J A, Sheikhi M, Li L, Guo W, Dai J N, Chen C Q and Ye J C 2019 Strain modulated nanostructure patterned AlGaN-based deep ultraviolet multiple-quantum-wells for polarization control and light extraction efficiency enhancement *Nanotechnology* **30** 9
[28] Lu H M, Yu T J, Yuan G C, Jia C Y, Chen G X and Zhang G Y 2012 Valence subband coupling effect on polarization of spontaneous emissions from Al-rich AlGaN/AlN Quantum Wells *Opt. Express* **20** 27384–92
[29] Northrup J E, Chua C L, Yang Z, Wunderer T, Kneissl M, Johnson N M and Kolbe T 2012 Effect of strain and barrier composition on the polarization of light emission from AlGaN/AlN quantum wells *Appl. Phys. Lett.* **100** 4
[30] Chuang S L 1995 *Physics of Optoelectronic Devices* (New York: Wiley)
[31] Chuang S L 1996 Optical gain of strained wurtzite GaN quantum-well lasers *IEEE J. Quantum Electron.* **32** 1791–800
[32] Rinke P, Winkelnkemper M, Qteish A, Bimberg D, Neugebauer J and Scheffler M 2008 Consistent set of band parameters for the group-III nitrides AlN, GaN, and InN *Phys. Rev. B* **77** 15
[33] Wetzel C, Takeuchi T, Yamaguchi S, Katoh H, Amano H and Akasaki I 1998 Optical band gap in $Ga_{1-x}In_xN$ ($0 < x < 0.2$) on GaN by photoreflection spectroscopy *Appl. Phys. Lett.* **73** 1994–6
[34] Ponce S, Jena D and Giustino F 2019 Route to high hole mobility in GaN via reversal of crystal-field splitting *Phys. Rev. Lett.* **123** 096602
[35] Jiang K, Sun X, Ben J, Shi Z, Jia Y, Wu Y, Kai C, Wang Y and Li D 2019 Suppressing the compositional non-uniformity of AlGaN grown on a HVPE-AlN template with large macro-steps *Crystengcomm.* **21** 4864–73
[36] Jiang K, Sun X, Ben J, Jia Y, Liu H, Wang Y, Wu Y, Kai C and Li D 2018 The defect evolution in homoepitaxial AlN layers grown by high-temperature metal-organic chemical vapor deposition *Crystengcomm.* **20** 2720–8
[37] Ben J, Shi Z, Zang H, Sun X, Liu X, Lu W and Li D 2020 The formation mechanism of voids in physical vapor deposited AlN epilayer during high temperature annealing *Appl. Phys. Lett.* **116** 251601
[38] Ben J, Sun X, Jia Y, Jiang K, Shi Z, Liu H, Wang Y, Kai C, Wu Y and Li D 2018 Defect evolution in AlN templates on PVD-AlN/sapphire substrates by thermal annealing *Crystengcomm.* **20** 4623–9
[39] Miyake H, Nishio G, Suzuki S, Hiramatsu K, Fukuyama H, Kaur J and Kuwano N 2016 Annealing of an AlN buffer layer in N-2-CO for growth of a high-quality AlN film on sapphire *Appl. Phys. Express* **9**
[40] Al Tahtamouni T M, Lin J Y and Jiang H X 2012 Optical polarization in c-plane Al-rich $AlN/Al_xGa_{1-x}N$ single quantum wells *Appl. Phys. Lett.* **101** 3
[41] Bryan Z, Bryan I, Mita S, Tweedie J, Sitar Z and Collazo R 2015 Strain dependence on polarization properties of AlGaN and AlGaN-based ultraviolet lasers grown on AlN substrates *Appl. Phys. Lett.* **106** 5
[42] Long H, Wang S, Dai J, Wu F, Zhang J, Chen J, Liang R, Feng Z C and Chen C 2018 Internal strain induced significant enhancement of deep ultraviolet light extraction efficiency for AlGaN multiple quantum wells grown by MOCVD *Opt. Express* **26** 680–6
[43] Reich C *et al* 2015 Strongly transverse-electric-polarized emission from deep ultraviolet AlGaN quantum well light emitting diodes *Appl. Phys. Lett.* **107** 142101